5.1 Introduction

To meet the increasing need for the next generation spintronic devices, multi-functional materials which respond to various external stimuli, e.g., magnetic field, electric field, pressure, etc. are required. Particular attention has been given to look for the materials showing strongly coupled magnetism and electrical behaviours [1-4]. In this regard, the materials with double perovskite (DP) structure i.e. $R_2BB'O_6$ (R= rare earth and B and B'= transition metal**)** are of particular importance owing to their diverse fundamental and fascinating physical properties including near room temperature ferromagnetism, large magneto-dielectric effect, giant magneto-resistance, giant exchange bias, magneto-caloric effect etc [3-6]. Hence, such compounds have provided new frontier in material research and opened up ample opportunities for a broad spectrum of potential applications including sensors, spin filter junctions, memory devices, etc. [7-8]. Depending upon the B/ B'-site ordering, the DPs are found to crystallize mainly into two types of structures: (1) the ordered monoclinic structure with P_{21}/n symmetry (2) the B-site disordered orthorhombic structure with Pnma symmetry [9-10]. Eventually, the ordered DPs show the ferromagnetic (FM) behaviour owing to 180^0 super-exchange interactions B^{2+}-O^{2-}-B'^{4+} (typically B= Co/Ni and B′=Mn) but co-existence of B^{3+}/B'^{3+} ions (as a disorder) introduces the competing anti-ferromagnetic (AFM) interactions [5,11]. However, despite the intense research interests and meticulous investigations on such DPs, complete understanding of its electronic structure is still far from well understood. Again, the self-ordering of the **B/B'** site ions in ordered DP occurs when these two ions have significant difference in their ionic radii and the charge states [9-10]. Conversely, B-site disorder occurs for same charge states of B-site ions. Eventually, site disorder of a system is known to have profound effects on its physical properties which offered a fertile ground for theoretical research and called for rigorous

experimental investigations world-wide [5,11-16]. Moreover, few members of the ordered FM DPs exhibit spin-phonon coupling due to existence of competing nature of spin and phonon degrees of freedom [6,9,16-17]. In fact, coupling between the magnetism (spin) and lattice (phonon) is one of the crucial mechanisms for the coupling between magnetic and electric orders in solids. Thus, to elucidate the magneto-electric coupling phenomena, probing the spin-phonon coupling can be an effective tool. For the strongly correlated oxide systems in which multi-functional properties are observed due to the presence of coupling between different properties, e.g., spin-phonon coupling, electron-phonon coupling etc., Raman spectroscopy can be a sensitive gauge for monitoring such coupled degrees of freedom [17-19,20].

Eventually, the Co/Ni/Mn-based ordered FM insulating DPs have been extensively studied in the past few years [5,10-11,15]. On the other hand, the studies on the Fe based DPs are relatively limited, and hence much more possibilities are there to explore its physical properties [21-25]. Hence, we have chosen a new Co/Fe based DP Pr2CoFeO6 (PCFO) for our study and we shall discuss its electronic structure and lattice dynamics property study in this chapter.

In fact, a comprehensive study deciphering the existence of spin-phonon coupling in such disordered AFM DP system PCFO is hitherto unreported, thus it can be interesting to study its temperature-dependent Raman spectra to unravel how magnetic ordering affects phonon modes in PCFO. Besides, Raman study is also helpful in getting an insight into the B-site cationic ordering in the system.

The local valance states of the B/B′ site ions are strongly correlated to its cationic ordering; thus a prior understanding of its electronic structure can eventually help in further explorations of the origins of its different properties. On the other hand, both the XPS and XAS are the widely used versatile and powerful techniques to probe the elemental

composition and their nominal chemical states of a compound. In XPS study of a system having open-shell ions, the coupling between the open-shell and a core electron vacancy bring out multiplet structure which can effectively reveal the electronic structure of it. Apart from the main photoelectron spectral lines in XPS, the accompanying satellite shake-up peaks, chemical shifts and relative intensities of the core level peaks can be used to get precise information of nominal valance states, ligand co-ordinations and other electronic structure considerations. In XAS, the incident X-ray photon excites an electron in the core level to an unoccupied conduction level following the intra-atomic dipole selection rule. Like XPS, the XAS is used for the analysis of the oxidation states of the elements of a material. However, additionally, XAS has an intrinsic capability to sense the spin-states of ions precisely. This information of spin state remains embedded in the same multiplet structure which is used to specify the presence of different charge states. Eventually, in the present PCFO system, one end member is $PrCoO_3$ belonging to the cobaltite $RCoO_3$ family which have drawn considerable attention due to its inherent spin degree of freedom in addition to the other degrees of freedom viz., charge, orbital and lattice [26-28]. This emerges due to the three different energetically (merely) degenerate possible spin configurations of the Co^{3+} ions i.e. low (LS $t_{2g}^6 e_g^0$), intermediate (IS $t_{2g}^5 e_g^1$) and high (HS $t_{2g}^4 e_g^2$) spin states. For $PrCoO_3$, it is still under debate whether the spin state remains in the low spin state (LS) or goes to higher spin states (high or intermediate) up to 300 K [28]. Although extensive studies on the electronic structure of the system $LaCoO_3$ can be found in literature, works on the $PrCoO_3$ system are particularly limited and needs much more efforts to understand its electronic structure. Unlike $LaCoO_3$ (absence of 4f electrons), $PrCoO_3$ contains two 4*f* electrons which effectively contribute in its valence band structure. Again, in $LaCoO_3$, the crystal field splitting is found to be of the order of exchange interactions. However, for $PrCoO_3$ system, substituting smaller ions Pr^{3+} in the place of La^{3+} essentially increases the chemical pressure

and this in turn transforms the structure from rhombohedral to orthorhombic symmetry leading to the lattice distortion. This is expected to have a direct effect on the hybridization process near Fermi level and thus affecting the bandwidth of the valance band. Also, the effective Co-O bond length in $PrCoO_3$ gets decreased and thus it is expected to enhance the crystal field splitting. This altered crystal field splitting energy competing with the Hund's coupling energy can also affect the spin states of the Co^{3+} ions. However, to date no report on the electronic structure of Pr_2CoFeO_6 is available in literature; this provoked us for investigating its electronic structure.

In the present work with PCFO, we have thoroughly investigated the room temperature electronic structure by XPS study and phonon behaviour by temperature dependent Raman measurements.

5.2 Experimental

5.2.1 Sample synthesis

The sample of Pr_2CoFeO_6 was prepared by standard solid state reaction route. The flow chart of its preparation steps is shown in below:

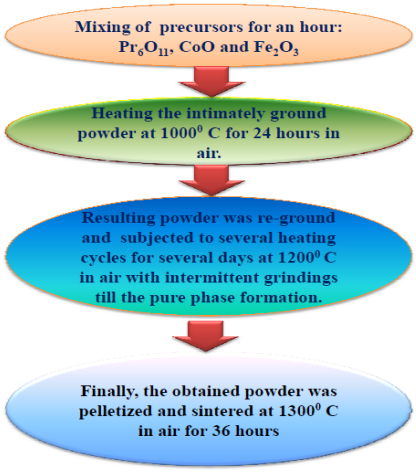

Figure. 5.1: *Flow chart of the sample preparation steps by solid state reaction route.*

The high purity (>99.99%) oxide powders of Pr_6O_{11}, CoO and Fe_2O_3 as precursors were taken in proper molar ratio and after intimately grinding for an hour subjected to an initial heat treatment at 1000^0 C for 24 hours in air. The resulting powder was then reground and was again subjected to several heating cycles at 1200^0C with intermittent grinding and reheating steps for several days. In the final step, the resulting powder thus obtained was pressed into pellets and sintered at 1300^0C for 36 hours followed by a slow cooling to room temperature. The Rietveld refinement of the X-ray diffraction (XRD) data recorded at 300 K confirmed that the system crystallized in single phase Pnma structure (Fig. 5.2).

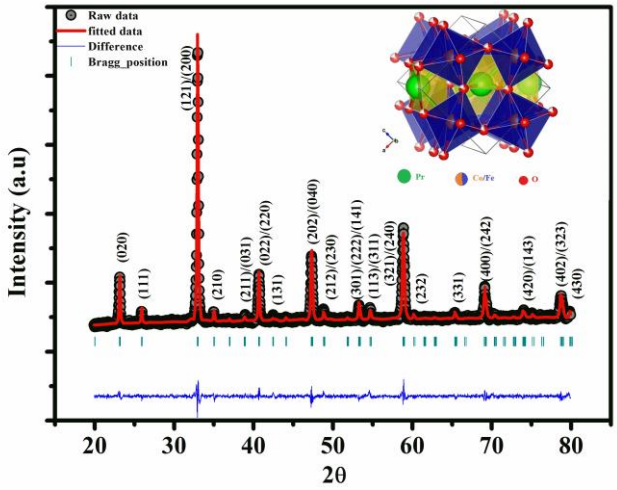

Figure. 5.2 : *XRD along with its Rietveld refinement at 300 K. Inset: Polyhedral representation of the crystal structure. The green and red balls are representing the Pr and O atoms. The blue octahedra refer to Co/FeO*$_6$.

5.2.2 Material characterization details:

The XRD data was recorded using a Rigaku miniflex II X-ray diffractometer. The XPS data was recorded by an Omicron multi-probe surface science system which is well-equipped with a hemispherical electron energy analyzer (EA 125) along with a monochromatic X-ray source Al-K_α line with photon energy 1486.70 eV. The average base pressure was maintained at a value of ~ 2.8×10^{-11} Torr. The total energy resolution as

calculated from the width of Fermi edge was about 0.25eV. The XAS measurements were performed at the BL14 beamline of Hiroshima Synchrotron Radiation Centre, Hiroshima University, Japan. The total electron yield (TEY) mode has been used as it requires relatively easy experimental setup and gives high signal to noise ratio. Raman spectra were recorded in a Renishaw inVia Raman spectrometer with 532 nm line of a diode pumped solid state laser delivering power of 5 mW mm^{-2}. To control the temperature of the sample, it was kept on a quartz sample holder which was put on the heating/cooling sample cell (THMS-600) connected to temperature control stage (TMS94). The incident laser beam was focused on the sample through the transparent window of the THMS-600 by a 50× short distance objective attached to the Leica DM 2500M microscope. Backscattering geometry was used to collect the scattered beam through the same objective, and a 2400 grooves/mm grating was used as the dispersion element. The spectra were recorded with a spectral resolution of ~1 cm^{-1}. The dc magnetization measurements were performed using a Quantum Design MPMS SQUID magnetometer.

5.3 Results and discussions

5.3.1 X-ray photoemission spectroscopy study:

We have investigated the electronic states near the Fermi level of PCFO by XPS study at 300 K. Figure. 5.3(a) shows the survey spectrum of PCFO system, wherein specifications of the all peaks have been assigned according to the National Institute of Standards and Technology (NIST) database. It reveals that Pr, Co, Fe, and O are present at the surface of PCFO. However, the presence of any other elements except C was not detected from the spectrum, thus confirming the purity of the sample. The presence of C can be attributed to the adventitious molecules absorbed at the surface from the air. We have analyzed the XPS data by correcting the observed binding energies of the elements by referencing the C *1s* line at

284.8 eV to eradicate the charging effect. Figure 5.3(b) depicts the core level XPS spectrum of Pr3d region which comprises of two main (spin-orbit coupling) peaks Pr($3d_{5/2}$) and Pr($3d_{3/2}$) at ~933.3 eV and ~953.7 eV respectively. Two additional exchange splitting peaks (ΔE~4.8 eV) are also observed at energies ~928.5 eV and ~948.9 eV [29]. These two exchange splitting peaks are produced due to the strong mixing of the final states (although in its ground state, Pr^{3+} has $4f^2$ configuration) $3d^9 4f^2$ and $3d^9 4f^3\underline{h}$ ($\underline{h}$ represents hole in O*2p* valance band) through the co-valency hybridization [29]. Another clear feature denoted by m can be clearly observed above Pr$3d_{3/2}$ main peak (such feature is absent in La*3d* XPS spectra). This feature m is seemingly associated to the multiplet effect [29]. All the above features strongly suggest the trivalent oxidation state of Pr ions. Moreover, for neutral Co atoms, Co *2s* peak appears at 925.1 eV which should lie at slightly higher energy for Co^{3+} ions [30]. However, the states Pr $3d_{5/2}$ and Co *2s* have a theoretical cross-sectional area ratio of ~8 [30]. Whereas, the integrated areas under the experimental XPS peaks at ~933.3eV and ~928.5 eV have a ratio of ~ 2.59. Thus, if we assume that 933.3 eV peak is arising due to the Pr$3d_{3/2}$ while 927.5 eV peak is due to the Co *2s* state, the area ratio of these two curves (~2.59) is in sharp contrast to the theoretically expected ratio (~8). Additionally, the theoretical area ratio of the main Pr*3d* and its exchange splitting peaks is 2:1 which is close to our observed value (2.59:1). Hence, the observed feature can be ascribed to the predominant contribution from Pr3d states.

Even though the XPS analysis is a surface sensitive technique but due to having the large mean free path of photoelectrons coming from cobalt (~ 1.5 nm for E_K^{in} =700eV), the Co*2p* XPS spectra has the ability to provide multiple information viz., charge and spin states, etc. Figure 5.3(c) depicts the core level Co*2p*XPS spectrum mainly consisting of two spin-orbit splitting peaks centered at ~779.6 eV ($2p_{3/2}$) and ~794.7 eV ($2p_{1/2}$). For Co-based compounds, the study of the XPS spectra is important since it contains shake-up satellite peaks which are

highly sensitive to cation valency, ligand co-ordination etc [31-33]. The underlying physics of the shake-up satellite process in the 2p core level XPS spectra involves the screening of a core-hole through charge transfer from the ligand or sp orbitals. In its process, of the two competing channels leading to the final (excited) states: one is associated to the screening of the core-hole via charge transfer from ligands to the 3d orbitals leading to the well-screened state i.e. the main photoelectron peak. The other channel leading to the poorly-screened state corresponds to the shake-up satellite peaks (here the charge compensation occurs via sp orbitals instead of ligands). Eventually, the Co*2p* XPS spectra for high spin Co^{2+} ions in CoO exhibit such strong satellite structures positioned at ~7 eV above main peaks. [31-33]. On the contrary, the low-spin Co^{3+} ions in octahedral co-ordination viz., Co_2O_3, $LiCoO_2$ etc typically do not show any charge-transfer satellite or show it with very low intensity (compared to the Co^{2+} in CoO) [32-33]. This happens for Co^{3+} due to the reduced charge transfer energy and enhanced Co*3d*-O*2p* hopping strength as compared to the Co^{2+} case. Hence, observation of the mere absence or very weak feature of such satellite peaks in our Co*2p* XPS spectrum further suggests the presence of octahedrally coordinated Co^{3+} ions [32-33]. Again, the spin-orbit coupling of the observed spectra (ΔE~15.1 eV) is also found to be consistent for Co^{3+} ions (as for Co^{2+} ions, it is ≥16 eV) [33].

In Fig. 5.3(d), the Fe *2p* XPS spectra of PCFO are shown. It comprises two main peaks, positioned at ~710.9 eV($2p_{3/2}$) and ~724.6 eV($2p_{1/2}$) with ΔE ~13.7 eV which are consistent with Fe ions with nominal valance state +3 [34]. Two shake-up satellite peaks marked as S_1 and $S_2$are observed at positions ~718.8 eV and ~732.9 eV respectively. In principle, these satellite peaks appear due to charge transfer between the ligand site (O^{2-}) and metal ion Fe^{3+}/Fe^{2+} site. Since, different Fe ions viz., Fe^{2+} and Fe^{3+} have different electronic configurations (d^6 and d^5), it raises the satellite peaks at different positions (thus treated as hallmark). The Fe*2p* XPS spectra containing Fe^{2+} ions always show satellite peaks at ~ 6 eV

higher than the main peaks whereas that containing Fe^{3+}ions show satellites at ~ 8 eV higher than main peaks [34]. Hence, trivalent Fe ions in PCFO can be inferred.

The core level O 1s spectra are shown in Fig. 5.3(e). The spectra consist of a strong peak at ~528.5 eV and a weak feature at ~ 530.8 eV. The first sharp peak at ~528.5 eV is the characteristic feature of the lattice oxygen "O^{2-}". However, the small peak at ~530.8 eV is ascribed to the oxygen species that contain fewer electrons due to the adsorption of oxygen leading to the formation of reduced electron rich species O_2^{2-} , O_2^- or O^- [35].

To get more insights into the electronic structure of Pr_2CoFeO_6, we have also recorded valance band (VB) spectra near the Fermi level (Fig. 5.3f). Furthermore, we have also simulated the experimental VB spectra with the theoretically obtained partial density of states (PDOS) (by DFT calculations) weighted by the atomic photoemission cross-section followed by binding energy dependent Lorentzian (accounting for the photo-hole lifetime broadening) and Gaussian (to account for the experimental resolution broadening) broadening which have been shown in Fig. 5.3(f) [36]. Both the experimental and the theoretical spectra showed the presence of weak spectral weight near the Fermi level indicating the insulating nature of the sample. Below Fermi level, the occupied spectral weight shows the most intense feature around ~2 eV for both of the spectra. This most intense feature is then followed by a shoulder like tail extending upto ~10 eV. The contrast between the most intense feature and its adjacent shoulder is conspicuous in the experimental spectra as compared to the theoretical one. This may be due to the errors incurred in the simulation of the experimental spectra which use the atomic values for the photoemission cross-sections which is a bad approximation for the photoemission matrix elements relevant for the itinerant valence states. As a matter of fact, the main contribution in forming the valence band is coming from O*2p*, Co*3d*, Fe*3d* and Pr*4f* orbitals. The most intense feature around ~2 eV is arising mainly due to

the hybridization of Co*3d*, Fe*3d* and Pr*4f* with O-2p orbitals with significant proportion being from the Pr4*f*. On the other hand, the feature near the Fermi level (0-1 eV) is mainly associated with the extended Co/Fe*3d* orbitals. While the broad shoulder like feature above the most intense feature can be mainly ascribed to the hybridization of O*2p* and Co/Fe*3d* states and other contributions, e.g. O*2p*-Co/Fe 4*sp* and O*2p*-Pr *5sd* oxygen bonding states.

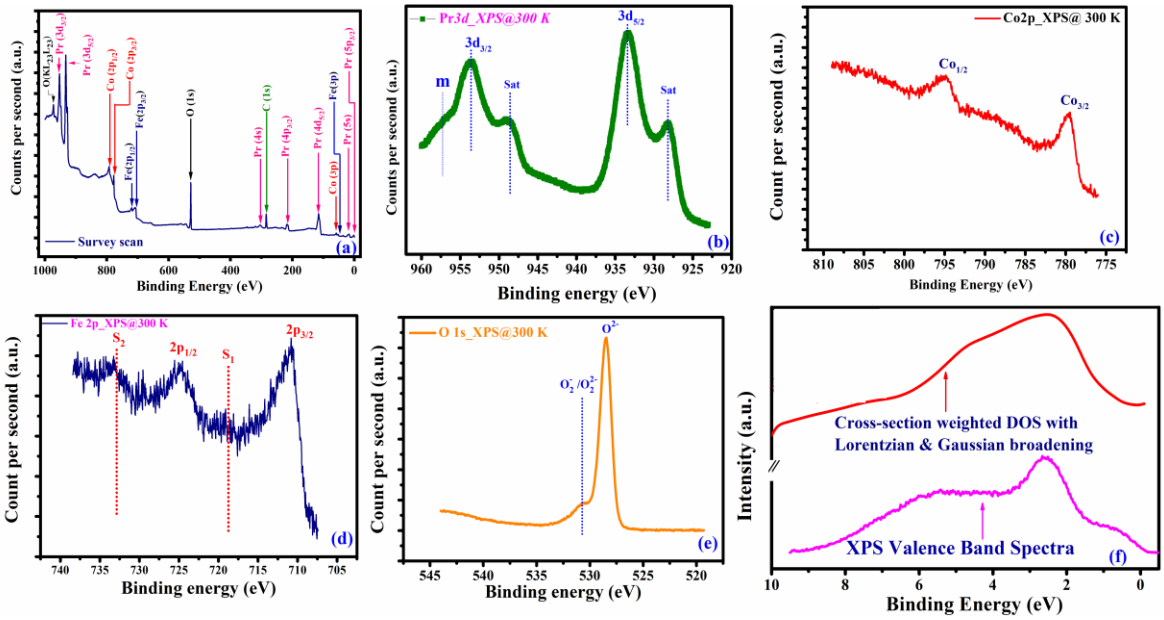

Figure. 5.3: *(a) XPS survey scan of PCFO. Core level spectra of Pr3d, Co2p, Fe2p, O1s are depicted in figures b, c, d and e respectively. Figure (f) represents the theoretical cross-section weighted DOS with Lorentzian and Gaussian broadening (upper panel) and XPS valance band spectra of PCFO (bottom panel).*

5.3.2 X-ray absorption spectroscopy (XAS) study:

Figure 5.4(a) demonstrates the Co *2p* XAS spectrum (at 300 K) related to the photo-absorption from Co*2p* core level to the Co *3d* unoccupied level. The spectrum comprises of two main peaks Co$L_3(2p_{3/2})$ and Co$L_2(2p_{1/2})$at ~780.7 eV and ~795.2 eV, respectively. The separation of these two peaks is associated to the spin-orbit (SO) coupling (ΔE~14.5 eV). The line shape and the peak positions of the observed Co*2p* XAS spectra clearly suggest presence of trivalent Co ions in PCFO which is consistent with XPS data analysis [27]. No trace of a

pronounced peak at ~ 777 eV corresponding to Co^{2+} ions can be observed from Fig. 5.4(a). This directly rules out any possibility of presence of any divalent Co ions in PCFO. Factually, the Co*2p* XAS spectra recorded at *L2-3* edge is extremely sensitive to the spin states since it involves the relevant valence shells directly. On looking at the L_2 edge of the Co*2p* XAS spectra, a narrow and relatively sharp peak can be observed which is similar to the feature observed in Co*2p* XAS for $LaCoO_3$ at 20 K [27]. This narrow and sharp L_2 peak at Co*2p* XAS is a hallmark for low-spin state (LS) of Co^{3+} ions, so it undoubtedly confirms the presence of LS Co^{3+} ions in PCFO at room temperature [27]. Factually, LS Co^{3+} state was also observed in another DP Ho_2CoFeO_6 [23].

Figure. 5.4(b) depicts the Fe*2p* XAS spectrum recorded at 300 K. The Fe*2p* XAS spectrum is ascribed to the transition of electrons from Fe*2p* to Fe*3d* states. The Fe *2p* XAS spectrum can be broadly divided into two peaks Fe$L_3(2p_{3/2})$ and Fe$L_2(2p_{1/2})$ positioned at ~ 710.2 eV and ~723.6 eV, respectively, the corresponding spin-orbit splitting energy is ΔE~ 13.4 eV. Due to crystal field splitting, each of the main L_3 and L_2 peaks is further split into e_g and t_{2g} doublet. These t_{2g} features can be observed in the form of a prominent shoulder and a peak just 1.6 eV below the main L_3 and L_2 peaks respectively. The formation of this t_{2g} and e_g splitting can be attributed to the localized nature of Fe *3d* electrons. Essentially, the spectral features are similar to the Fe*2p* XAS spectra of the extensively studied Fe_2O_3 system, where the nominal valency of the Fe ions is +3 [37]. The Fe*2p* XAS spectral feature excludes similarities from the spectral features as typically seen in metallic Fe, FeO or Fe_3O_4, suggesting absence of any mixed-valence states [37]. It can be further noted that for Fe^{3+} ions sitting in the tetrahedral co-ordination, the L_3 and L_2 peaks are not split into e_g-t_{2g} doublet [38]. On the other hand, for the Fe^{3+} ions sitting in the octahedral co-ordination, it splits into e_g and t_{2g} which are separated by 1.6 eV [38]. Hence, the octahedral co-ordination of Fe^{3+} ions can be inferred for PCFO. Thus, the XAS data is in well-agreement with XPS results.

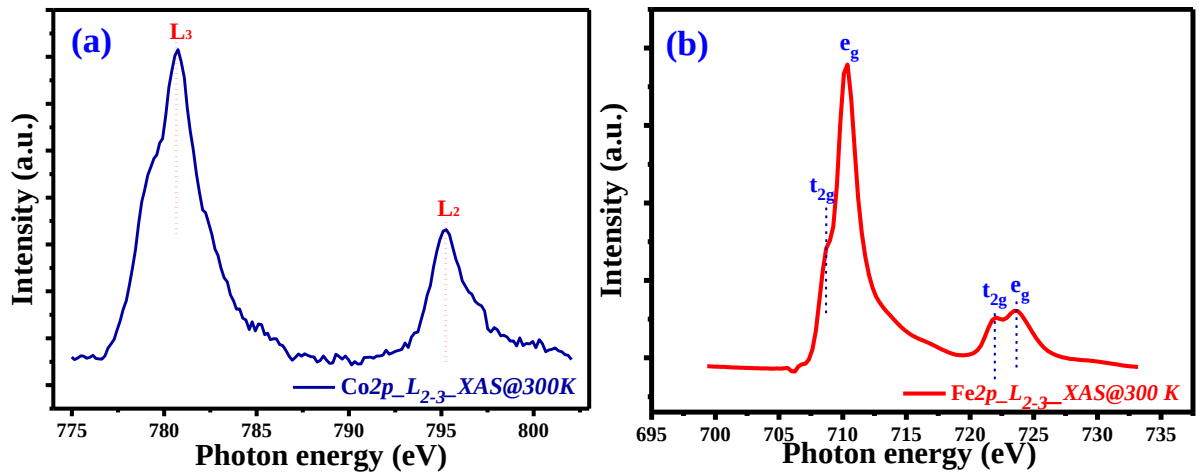

Figure. 5.4: *(a) and (b) show the room temperature XAS spectra at CoL2-3 and FeL2-3 edges respectively.*

5.3.3 Temperature-dependent Raman study:

The diffraction techniques are helpful for probing the basic crystal structure and its symmetry while the Raman spectroscopy is a unique tool to examine the changes in the local or/and dynamic structural symmetry, local disorder, cationic ordering, etc. [9,10,17-19]. However, for the simple cubic $Pm\bar{3}m$ structure of ideal perovskites, all the atoms are centro-symmetrically positioned, and hence no Raman-active phonon modes are found in their Raman spectra. In contrast for the Pnma structure, the distortion caused by the motion of the oxygen atoms around the B-site ions (in BO_6) or shifts in R lifts the degeneracy of the Raman modes, and few additional Γ-point phonons become Raman allowed [39]. The symmetry analysis by group theory predicts that there are 60 possible Γ-point phonon modes in such compounds with orthorhombic structure (Pnma). Of these possible modes, only 24 are found to be Raman allowed while among the rest, 25 are infrared allowed, 3 are acoustic translational and 8 are inactive silent modes. The Raman active modes are written in irreducible representation as $\Gamma_g = (7A_g+5B_{1g}+7B_{2g}+5B_{3g})$, where A_g modes correspond to the

stretching vibrations of BO_6 octahedra and B_g modes refer to the anti-stretching modes of vibration from the same source.

In the Fig. 5.5 (a), we have shown the experimental Raman spectra (i.e., the scattering intensity variation with the Raman shift) recorded at different temperatures ranging from 300 K to 80 K for Pr_2CoFeO_6. It can be seen from the Fig. 5.5 (a) that of many weak Raman bands, two prominent bands positioned at ω_1~ 435 cm^{-1} and ω_2~ 650 cm^{-1} are observed for all the temperatures. Typically, the phonon modes arising due to the motion of the heavy rare earth ions appear below the 200 cm^{-1}, and the modes observed above 300 cm^{-1} are solely due to the motion of light oxygen ions. As already stated the Co/Fe (B-site) ions are centrosymmetric hence they do not contribute to these modes. Thus, both of the observed peaks are associated to the oxygen motion in Co/FeO_6 octahedra. Observing the similarities between the observed Raman spectra of PCFO to that of the other earlier reported spectra of perovskites and double perovskites oxides, bands observed at ~435 $cm^{-1}$and ~650 cm^{-1} can be attributed to the anti-stretching and stretching (or breathing) vibrations of the Co/FeO_6 octahedra respectively [9,10,16,19,39-42]. Illiev et al. have explicitly shown by the lattice dynamical calculations that the lower energy band ω_1 involves both the bending and anti-stretching vibrations whereas the higher energy band ω_2 arises purely due to the stretching vibrations **[**41]. It is a comprehensible fact that for the fully disordered DPs; the number of Raman excitation peaks should remain the same as for the single perovskite, i.e. RBO_3 or $RB^{I}O_3$**.** However, the only noticeable change that can be observed is the change in the phonon frequency, and their peak widths arising due to the changes occurred in the average force constants (due to random B-O/ B^{I}-O bonds) and their phonon lifetimes [40,42]. As PCFO has B-site disordered orthorhombic structure, the observed broadness in both of the bands ω_1 and ω_2 can be ascribed to the random site distribution of the Co/Fe ions. Moreover, another feature that can be noted in the peaks (Fig. 5.5 a) is the asymmetry in its shapes.

Eventually, due to the presence of cationic disorder in PCFO, the different B/B′-O vibrations (these unresolved contributions originating from different B/B′-O_6 octahedral co-ordinations) will lie close in energy leading to the formation of an asymmetric band envelope.

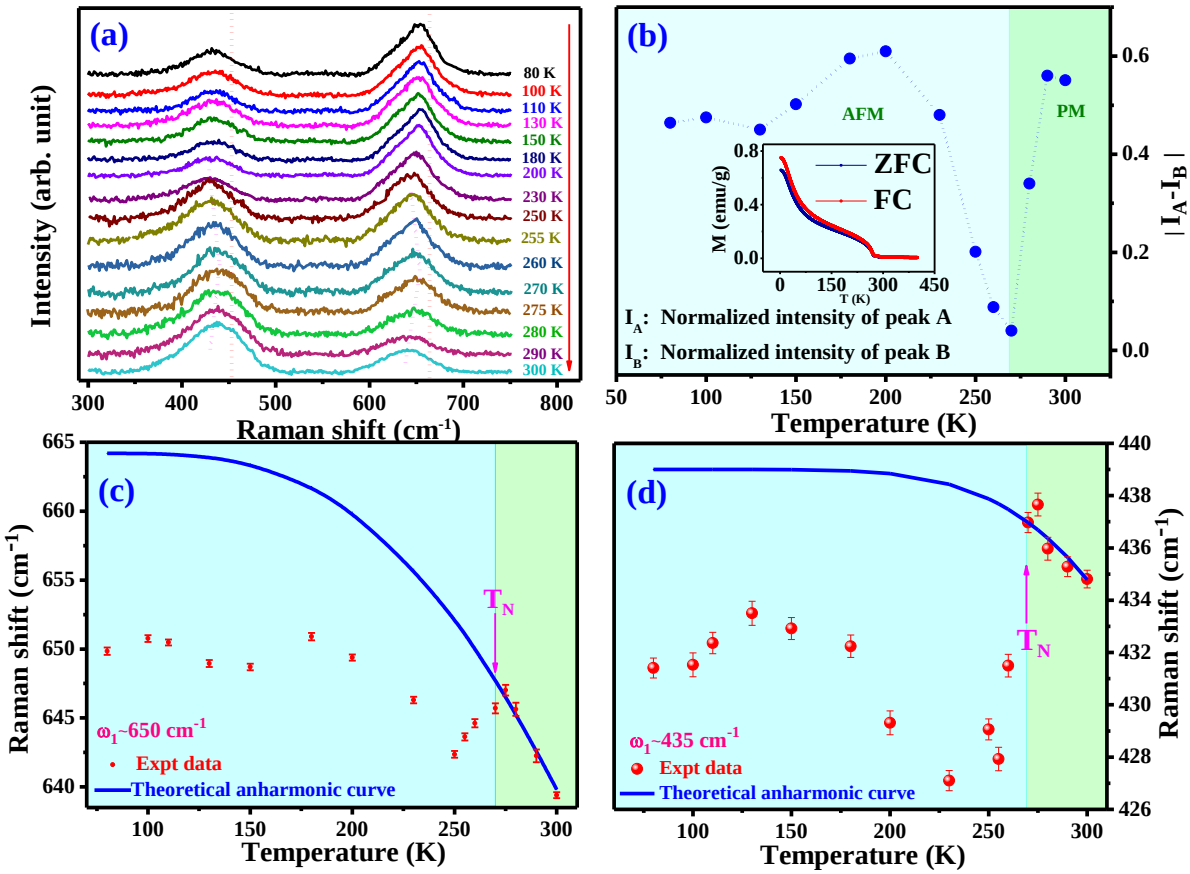

Figure. 5.5: *(a) Raman spectra at different temperatures. (b) Relative height variation of two modes with temperature and its inset shows the temperature dependent magnetization ZFC and FC curves. Anharmonic fit to the "thermal variation of Raman shift" for stretching (c) and anti-stretching (d) modes respectively.*

As a matter of fact, ordered DP systems ($P2_1/n$) e.g., La_2CoMnO_6, Pr_2CoMnO_6, Nd_2CoMnO_6, Y_2CoMnO_6, and Y_2NiMnO_6 etc. exhibit additional number of low intensity Raman modes (along with the two main intense stretching and anti-stretching modes) which

are attributed to the B-site cationic ordering in the system [6,43,44]. Factually, in the ordered DPs, the effective lattice parameter increases due to the cationic ordering leading to a Brillouin zone folding which essentially gives rise to additional new Γ-point Raman modes [40]. Moreover, for the epitaxial thin film of the DP compounds, a clear peak splitting (which is typically considered as a hallmark for cationic B-site ordering) is observed in both of the stretching and anti-stretching modes [9,10,40]. On the contrary, for the compounds with disordered orthorhombic (Pnma) structures show less number of Raman modes as compared to that for ordered monoclinic ($P2_1/n$) structures [19,43]. As a matter of fact, we could identify only two main broad peaks $\boldsymbol{\omega_1}$~435 cm^{-1} and $\boldsymbol{\omega_2}$~650 cm^{-1} for PCFO, suggesting towards the random site distribution of the Co/Fe atoms which is consistent with its electronic structure (Co/Fe are in same +3 oxidation states) [25].

On the other hand, the DPs containing R-site ions of large ionic radii usually show smaller number of Raman modes. This is because large R-ions cause smaller octahedral tilts and relatively small distortions which lead to the rise of Raman modes at low wave numbers but of weaker intensities as compared to that of DPs with smaller R-ions (causing large octahedral distortions). Thus, for DPs with smaller R-ionic radii show more resolvable Raman modes as compared to the DPs with large ionic radii [43,44]. Hence, the absence of such additional Raman modes for PCFO can also be elucidated based on the large ionic radii of the Pr-ions.

Raman spectra at different temperatures ranging from 300 K down to 80 K have been recorded to study the effect of magnetic ordering upon the lattice vibration (Fig. 5.5a). To explore the impact of the temperature on the relative intensities of the two Raman modes (stretching and anti-stretching), we have normalized each of the Raman spectra concerning the most intense peak. Interestingly, the intensities of the two bands ω_1 and ω_2 vary

differently with temperature. The intensity of the most intense peak at room temperature, i.e., the anti-stretching mode (**ω_1**) remains almost constant throughout the temperature range whereas that of stretching mode (ω_2) keeps increasing with decreasing temperature. This behaviour is scarce and interesting since the Raman intensity usually increases with decreasing temperatures owing to the reduced phonon scattering at low temperatures. Figure. 5.5(b) shows the plot of relative intensity $|I_{\omega 1}- I_{\omega 2}|$ as a function of temperature. Interestingly, as the temperature lowers below 270 K, the intensities of both the Raman modes ω_1 and ω_2 become merely equal. Below 270 K, the intensity of **ω_2** peak starts dominating over that of the **ω_1** peak. Again, the temperature variation of dc magnetization study of PCFO following the zero field cooled and field cooled protocols under applied magnetic field of 250 Oe has shown a drastic jump below~ 270 K, suggesting for a magnetic transition (inset of Fig. 5.5b). Hence, it indicates that the onset of magnetic ordering is affecting the phonon modes, thus leading to the observed anomalous behaviour of their thermal intensity variations.

To further confirm whether the magnetic spin ordering affects the lattice vibrations, we have investigated the "temperature variation of the Raman excitation frequencies for both the modes i.e. ω_1 and ω_2" (Fig. 5.5 c &d). Since, for the whole temperature range, no additional Raman mode could be observed, it undoubtedly ruled out the possibility of any global structural transition. Under such condition, the temperature variation of the phonon excitation wave number should follow the anharmonic behaviour (due to usual thermal lattice contraction) which is described by the following expression [45]:

$$\omega_{anh}(T) = \omega_0 - C\left(1 + \frac{2}{e^{\frac{\hbar\omega_0}{K_B T}} - 1}\right);$$

Where ω_0 and C are the adjustable parameters, T is the temperature, ħ is reduced Planck's constant and K_B is the Boltzmann's constant. According to this function, the phonon frequency of a particular mode should exhibit gradual hardening with decreasing temperature and reach a plateau at sufficiently low temperatures. From Fig. 5.5(c-d), such phonon mode hardening down to the temperature T_N~ 270 K can be observed for both of the stretching and anti-stretching modes. Thus, it clearly suggests that anharmonicity is playing a dominant role in the temperature dependence of PCFO's phonon modes. Interestingly, it is discernible from Fig. 5.5(c-d) that both the stretching and anti-stretching modes, i.e., ω_2 and ω_1 deviate from the anharmonic behaviour below magnetic ordering temperature T_N. However, for the stretching mode ω_2, the theoretical curve attains the plateau region after going down to sufficiently low temperature < 150 K above which it continues the hardening while the experimental curve shows a dramatic slope change and exhibits anomalous softening below T_N (Fig. 5.5c). On the other hand, as evident from Fig. 5.5(d) the anti-stretching mode shows relatively larger deviation from anharmonic behaviour by showing more pronounced anomalous softening below T_N which is typically observed due to the spin-phonon coupling in other systems [6,16,41-44, 46-48]. Thus, these observations of anomalous softening of phonon modes (near T_N) involving vibrations of magnetic Fe ions indicate towards effective modulation in the lattice vibrations due to the magnetic ordering, thus leading to the spin-phonon coupling (Co^{3+} ions are non-magnetic and hence will not participate in magnetic ordering). However, in most of the perovskite compounds exhibiting spin-phonon coupling, such anomalous phonon softening was observed only in the stretching mode. On the contrary, the above results suggest that for PCFO at least two phonon modes are exhibiting the spin-phonon coupling and thus it eventually places this system amongst the rare materials.

It is pertinent to mention here that magnetostriction effect can also affect the phonon frequency (by altering the unit cell volume and lattice constants) leading to the anomaly in its

temperature variation [43,44,47-49]. Thus, it is crucial to confirm whether it is the spin-phonon coupling or the magnetostriction which one is causing the observed phonon anomaly. As a matter of fact, the full width at half maximum (FWHM) or line width of the relevant phonon modes remain unaffected by the subtle changes occurred in the volume/lattice parameters caused by magnetostriction effect. On the contrary, FWHM is related to the process of the phonon delay (i.e., lifetime) and thus can be affected by the spin-phonon coupling showing anomaly across magnetic transition [48]. Hence, we have investigated the thermal variation of the FWHM of the two modes (ω_2 and ω_1) as shown in Fig. 5.6 (a-b).

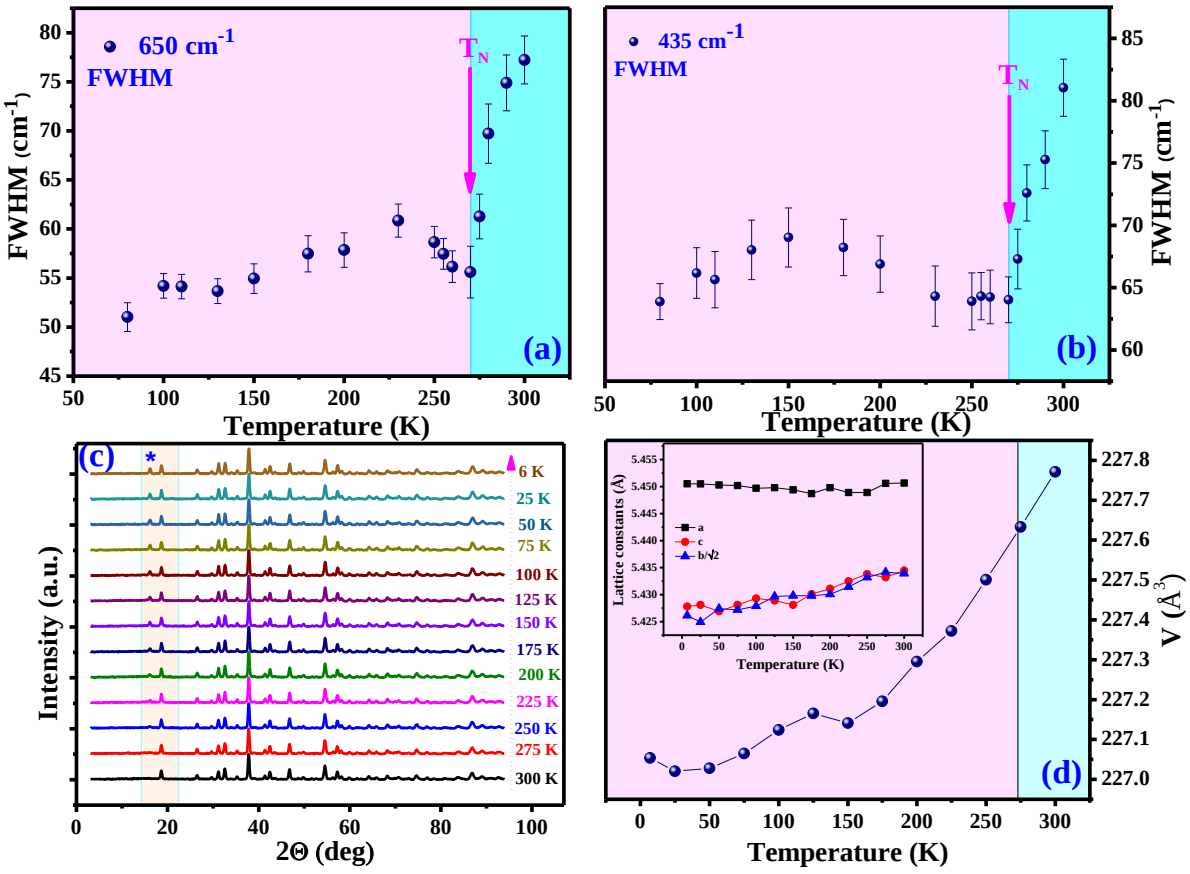

Figure. 5.6: *(a) and (b) Variation of FWHM with temperature for stretching and anti-stretching modes respectively. (c) Neutron diffraction at different temperatures. (d) Temperature variation of cell volume. Inset: thermal variation of lattice volume and lattice constants (a, b/√2 and c).*

Interestingly, for both of the modes, their FWHM showed an anomalous broadening below T_N~270 K and thus showed clear deviation from the expected anharmonic behaviour (i.e., monotonous increase in phonon lifetime or decrease in FWHM with decreasing temperature due to anharmonic perturbations) [48,49]. In this case, the observed temperature dependence of phonon line-widths cannot be explained by anharmonic behaviour alone. Thus, the observed anomalous FWHM broadening can be realized by the decrease in the phonon lifetime beyond T_N which is related to activation of some additional phonon decay modes due to entanglement of phonons with underlying long range magnetically ordered spins. Generally the phonon lifetimes are changed mainly due to two reasons (1) spin-phonon coupling and (2) electron-phonon coupling [20,48,49]. However, the present XPS study showed it to be an insulator which readily discards the possibility of electron-phonon coupling. Thus, the observation of FWHM anomaly can univocally be ascribed to the spin-phonon coupling in PCFO.

However, to further ascertain the absence of the role of magnetostriction effect in the observed phonon anomaly, we have investigated the temperature variation of the unit cell volume and the lattice parameters (Fig. 5.6d). The lattice parameters were obtained by refining the temperature dependent neutron diffraction (ND) data by Rietveld method (Fig. 5.6c). It can be noted that a magnetic reflection (011) (marked by *) starts appearing at ~16^0 below T_N which is suggesting the onset of long-range ordering in PCFO. The magnetostriction effect is typically manifested in the form of a remarkable anomaly in the volume and/or lattice parameter data across T_N, which provides a shred of direct evidence for this effect [48-50]. However, as evident from the Fig. 5.6d, no such remarkable anomaly can be observed in the volume and lattice parameters curves. Hence, it directly rules out the possibility of magnetostriction effect causing the observed phonon anomaly across T_N.

Therefore, all these above facts unambiguously establish the presence of the strong interplay among the microscopic degrees of freedom viz., spin and phonon in this system.

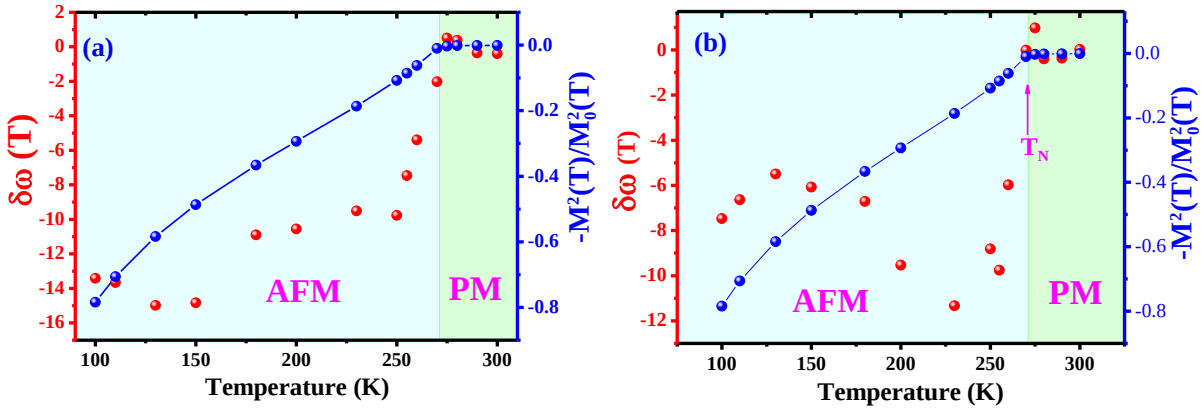

Figure. 5.7: *(a) and (b) Temperature variation of $\delta\omega(T)$and $(M(T)/M_0)^2$ for the stretching and anti-stretching modes respectively.*

Moreover, according to the mean field approximation when the long-range magnetic ordering sets in a structure, it induces a renormalization of the phonon frequency [18,19,44,46,47]. The phonon renormalization is found to be proportional to spin-spin correlation function ($< S_i . S_j >$), where S_i and S_j are denoting the nearest neighbour spins situated at ith and jth sites. The change in the phonon frequency due to this renormalization follows the same trend as the normalized magnetization leading the following formula:

$$\delta\omega(T) = \omega(T) - \omega_{anh}(T) = \left(\frac{M^2(T)}{M_0^2}\right)$$

, where M(T) represents the average magnetization at temperature T and M_0 is the saturation magnetization. The difference between the observed and theoretical anharmonic fitted data is

denoted by $\delta\omega(T)$. Hence, to further investigate the spin-phonon coupling, we have plotted the temperature variation of $\delta\omega(T)$and $(M(T)/M_0)^2$ for both the phonon modes (Fig. 5.7 a-b). As evident from the figures, $\delta\omega(T)$ and $(M(T)/M_0)^2$ follow a similar trend showing a downturn nearly at the same temperature (T_N ~270 K). This gives further confirmation that there is interplay between the lattice dynamics and the magnetic excitation via strong spin-phonon coupling in the system. However, for both the modes, $\delta\omega(T)$ and $(M(T)/M_0)^2$ do not overlap with each other. This can be presumably attributed to the existence of multiple magnetic phases in the system viz., AFM, FM, and spin glass phases which contributes towards different exchange interactions (both with values and signs) which in turn contribute differently in phonon renormalization [43,44,47]. Similar deviations from mean field theory were observed in few other systems viz., Y_2CoMnO_6, La_2CoMnO_6,$Sr_{0.6}Ba_{0.4}MnO_3$, etc. where complex FM/AFM and/or spin glass states co-exist, thus adding more complexity in the spin-phonon coupling process [43,44,47]. However, we hope that the present work may provoke theoretical studies to understand the spin ordering driven altered phonon behaviours in such site-disordered double perovskites. Further study on its single crystal or epitaxial thin film may be helpful to understand more about the intriguing underlying physics in it.

5.4 Conclusion

To summarize, we have investigated the electronic structure of PCFO by analyzing the XPS and XAS spectra at 300 K. Both the data analysis supported each other and unanimously confirmed the nominal oxidation states of B-site cations (i.e. Co, and Fe) to be +3 which in turn predicts towards a B-site disordered structure of PCFO. The XPS analysis yielded the trivalent valence states for the Pr ions. The XPS valence band spectra analysis showed the absence of electronic states at the Fermi level, thus suggesting an insulating nature of the system. Moreover, the XPS valence band spectra have been compared with the theoretically

(DFT) obtained cross-section weighted partial density of states followed by Lorentzian (lifetime) and Gaussian (instrumental) broadening. The Raman spectra analysis yielded a random distribution of B-site ions (Co/Fe) which is primarily triggered by the same charge states of the relevant ions. Moreover, the anomalous behaviour observed in the relative intensities of the stretching and anti-stretching Raman modes across T_N indicated the interplay of the spins and phonons in PCFO. Interestingly, both the Raman modes showed anomalous softening below T_N and deviated from anharmonic behaviour, thus confirming the existence of spin-phonon coupling for at least two modes. Besides, the temperature variation of the line widths of these two modes also showed remarkable anomaly below T_N which gave further confirmation of the strong coupling between spin and phononic degrees of freedom. Again, no anomaly in the lattice volume or lattice constants (a, b and c) across T_N could be observed in their temperature variation as obtained from neutron diffraction data analysis. This unambiguously confirmed the absence of magnetostriction effect in the observed phonon anomaly, thus, in turn, established the existence of the spin-phonon coupling in the system. Observation of such spin-phonon coupling for at least two phonon modes is very scarce for such compounds which eventually place it amongst the rare materials.

References:

1. S.W. Cheong and M. Mostovoy, Nat. Mater. **6**, 13 (2007).
2. Y. Kitagawa et al., Nature Mater. **9**, 797 (2010).
3. K.I. Kobayashi, T. Kimura, H. Sawada, K. Terakura and Y. Tokura, Nature,**395**, 677 (1998)
4. N. S. Rogado, J. Li, A. W. Sleight, and M. A. Subramanian, Adv. Mater. **17**, 2225 (2005). (LNMO) and references therein.
5. D. Choudhury, P. Mandal, R. Mathieu, A. Hazarika, S. Rajan, A. Sundaresan, U.V. Waghmare, R. Knut, O. Karis, P. Nordblad, and D. D. Sarma, Phys. Rev. Lett **108,** 127201 (2012) and references therein.
6. R. B. M. Filho, A. P. Ayala, C. W. de A. Paschoa, App. Phys. Lett. **102**, 192902 (2013)
7. W. Eerenstein, N. D. Mathur, and J. F. Scott, Nature, London **442**, 759 (2006) and references therein.
8. R. Ramesh and N. A. Spladin, Nature Mater. **6**, 21 (2007)
9. K. D. Truong, M. P. Singh, S. Jandl, and P. Fournier, Phys. Rev. B **80**, 134424 (2009) and references therein.
10. M. P. Singh, K. D. Truong, S. Jandl, and P. Fournier, Phys. Rev. B **79**, 224421 (2009)
11. R. I. Dass and J. B. Goodenough, Phys. Rev B **67**, 014401 (2003)
12. M. G. Hernández, J. L. Martínez, M. J. M. Lope, M.T. Casais and J. A. Alonso, Phys. Rev. Lett. **86**, 2443 (2001).
13. A. S. Ogale, S. B. Ogale, R. Ramesh, and T. Venkatesan, App. Phys. Lett. **75**, 537 (1999).
14. A. K. Pramanik and A. Banerjee,Phys. Rev. B **81**, 024431 (2010)

15. J. Blasco, J. García, G. Subías, J. Stankiewicz, J.A. Rodríguez-Velamazán, C. Ritter, J.L. García-Muñoz, and F. Fauth, Phys. Rev. B **93**, 214401 (2016).
16. H.S. Nair, D. Swain, H. N., S. Adiga, C. Narayana, and S. Elzabeth, J. App. Phys. **110**, 123919 (2011).
17. K. D. Truong, M. P. Singh, S. Jand and P Fournier, J. Phys.: Condens. Matter 23052202 (5pp) (2011)
18. E. Granado, A. Garcia, J. A. Sanjurjo, C. Rettori, I. Torriani, F. Prado, R. Sánchez, A. Caneiro, and S. B. Oseroff, Phys. Rev. B **60**, 11879 (1999)
19. J. Laverdiere, S. Jand, A. A. Mukhin, V. Yu. Ivanov,V. G. Ivanov and M. N. Iliev, Phys. Rev. B **73**, 214301 (2006)
20. R. Gupta, A. K. Sood, P. Metcalf, and J. M. Honig, Phys. Rev. B **65**, 104430 (2002)
21. C. Ganeshraj, R. N. Mahato, D. Divyaa, and P. N. Santhosh, J. Appl. Phys. **107**, 09E305 (2010)
22. N. Das,S.Singh,A. G. Joshi,M. Thirumal, V. R. Reddy, L. C. Gupta, A. K. Ganguli, Inorg. Chem. **56**, 12712 (2017).
23. G. R. Haripriya, H.S. Nair, R. Pradheesh, S. Rayaprol, V. Siruguri, D. Singh, R. Venkatesh, V. Ganesan, K. Sethupathi, and V. Sankaranarayanan, J. Phys.: Condens. Matter. **29**, 475804 (2017).
24. S. Chakraverty, A. Ohtomo, D. Okuyama, M. Saito, M. Okude, R. Kumai, T. Arima, Y. Tokura, S. Tsukimoto, Y. Ikuhara, and M. Kawasaki, Phys. Rev. B 84, 064436 (2011).
25. G. R. Haripriya, C. M. N. Kumar, R. Pradheesh, L. M. Martinez, C. L. Saiz, S. R. Singamaneni, T. Chatterji, V. Sankaranarayanan, K. Sethupathi, B. Kiefer, and H. S. Nair, Phys. Rev. B 99, 184411 (2019)

26. C. Zobel, M. Kriener, D. Bruns, J. Baier, M. Gru¨ninger, and T. Lorenz, Phys. Rev. B **66**, 020402 (R)(2002).

27. M.W. Haverkort, Z. Hu, J.C. Cezar, T. Burnus, H. Hartmann, M. Reuther, C. Zobel, T. Lorenz, A. Tanaka, N.B. Brookes, H.H. Hsieh, H.-J. Lin, C.T. Chen, and L.H. Tjeng, Phys. Rev. Lett. **97**, 176405 (2006).
28. J. Yu, D. Phelan, and D. Louca, Phys. Rev B **84**, 132410 (2011) and references therein.
29. H. Ogasawara, A. Kotani, R. Potze, G. A. Sawatzky, B. T. Thole, Phys. Rev. B **44**, 5465 (1991) and references therein.
30. S K Pandey, Ashwani Kumar, SMChaudhari and A V Pimpale, J. Phys.: Condens. Matter 18, 1313 (2006)
31. J. van Elp, J. L. Wieland, H. Eskes, P. Kuiper, G. A. Sawatzky, F.M. F. de Groot, and T. S. Turner, Phys. Rev. B **44**, 6090 (1991) and references therein.
32. S. Laureti, E. Agostinelli, G. Scavia, G. Varvaro, V. Rossi Albertini, A. Generosi, B. Paci, A. Mezzi, S. Kaciulis, App. Surf. Sci. **254,** 5111 (2008) and references therein.
33. C. A. F. Vaz, D. Prabhakaran, E. I. Altman, and V. E. Henrich, Phys. Rev. B **80**, 155457(2009)
34. T. Yamashita and P. Hayes, App. Surf. Sci. **254**, 2441 (2008).
35. G. U. Kulkarni, C. N. R. Rao, and M. W. Roberts, J. Phys. Chem. **99**, 3310 (1995).
36. J. J. Yeh and I. Lindau, Atomic data and nuclear data tables **32**, 1-155 (1985)
37. D. H. Kim, H. J. Lee, G. Kim, Y. S. Koo, J. H. Jung, H. J. Shin, J.Y. Kim, and J.S. Kang, Phys. Rev. B **79**, 033402 (2009).
38. M. Krishnan, Ultramicroscopy **32**, 309 (1990).
39. M. N. Iliev,M. V. Abrashev, H.-G. Lee,V. N. Popov, Y. Y. Sun, C. Thomsen, R. L. Meng and C. W. Chu, **57**, 2872 (1998).

40. M. P. Singh, K. D. Truong, S. Jand, and P. Fournier, J. App. Phys. **107**, 09D917 (2010) and references therein.
41. M. N. Iliev, M. V. Abrashev, A. P. Litvinchuk, V. G. Hadjiev, H. Guo, and A. Gupta, Phys. Rev. B 75, 104118 (2007)
42. H. Guo, J. Burgess, S. Street, A. Gupta, T. G. Calvarese and M. A. Subramanian, App. Phys. Lett. **89**, 022509 (2006)
43. D. Kumar, S.Kumar,V. G. Sathe, Solid State Commun. **194,** 59(2014)
44. R. X. Silva, M. C. Castro Júnior, S. Yanez-Vilar, M. S. Andujar, J. Mira, M. A. S. Rodriguez, C. W. A. Paschoal, J. Alloy. Compd. **690,**909e915 (2017)
45. M. Balkanski, R. F. Wallis, and E. Haro, Phys. Rev. B **28**, 1928 (1983).
46. P. K. Pandey, R. J. Choudhary, D. K. Mishra, V. G. Sathe, and D. M. Phase, App. Phys. Lett. **102**, 142401 (2013)
47. R. Rawat, D.M. Phase, R.J. Choudhary,J.Magn. Magn. Mater. **441,**398 (2017)
48. A. Nonato, B. S. Araujo, A. P. Ayala, A. P. Maciel, S. Yanez-Vilar, M. Sanchez-Andujar, M. A. Senaris-Rodriguez, and C. W. A. Paschoal, App. Phys. Lett. **105**, 222902 (2014)
49. V. S. Bhadram, B. Rajeswaran, A. Sundaresan and C. Narayana, Euro. Phys. Lett. **101,**17008 (2013).
50. M. S.-Andujar, S.Y.-Vilar, N. Biskup, S.C.-Garcia, J. Mira, J. Rivas, M. A. S.-Rodriguez, J. Magn. Magn Mater. **321,** 1739 (2009).